sciendo

Geologos 30, 2 (2024): 119–136
https://doi.org/10.14746/logos.2024.30.2.11

GEOLOGOS

Structural and mineralogical mapping using multispectral satellite data (Aster, Landsat 8 OLI, and Sentinel 2B) combined with field work in the Western High Atlas, Morocco

Nouhaila Elbakhouch*, Hassan Ibouh, Ahmed Touil, Driss Chafiki

Department of Earth Sciences, Faculty of Science and Technology, Cadi Ayyad University, Marrakesh, Morocco
*corresponding author, e-mail address: nouhaila.elbakhouche@gmail.com

Abstract

The Tighardine area in the Western High Atlas Massif is composed of rocks ranging in age from Neoproterozoic to Cenozoic. The area is intensely deformed with a multidirectional diversity of faults and also hosts a polymetallic ore deposit (Tighardine mine) and prospects of significant economic value, some of which are related to fault structures. In order to identify favourable areas of mineral deposition, structural and mineralogical mapping using satellite images was conducted in this region. For this purpose, various remote sensing approaches were employed on images from Landsat 8 OLI, Sentinel 2 and ASTER sensors. The process started with lineament extraction methods so as to identify faults manually from satellite images. Principal component analysis (PCA) and the optimal indexing factor (OIF) were used to achieve good discrimination of lithological units. Additionally, several band ratios were applied to ASTER, Landsat 8 OLI and Sentinel 2, in order to derive multiple maps corresponding to hydrothermal alteration zones. Analysis of the results from the obtained maps and their overlay with field data has allowed us to: (i) identify three main structural orientations. The most frequent and longest is the NE–SW direction, which coincides with the principal mineralised horizon of the Tighardine deposit. Results suggest an extension of this horizon towards the south-west at the Ait Zitoune and towards the west in the Ait Hsayn region. Two new fault set has been identified by remote sensing: NW-SE fracture, generally of Mesozoic-Cenozoic age, and an E-W fractures trend, particularly developed in the Neoproterozoic basement and considered of Ediacaran age; (ii) highlighting two potential mineralisation zones: in the Ediacaran basement, revealing alterations of silica, dolomite, clay minerals, iron oxide and alunite-kaolinite-pyrophyllite, hosting the main mineralisation axis (Tighardine mine); in the northern part corresponding to the overthrust zones of Cambrian onto Cenozoic formations.

Keywords: Mineralogical mapping, structural mapping, OIF, PCA, Tighardine area

1. Introduction

The Tighardine region is part of the Western High Atlas Massif (WHAM), which is located along the northern edge of the West African Craton and forms the junction of the Pan-African Anti-Atlas Range and the Mesetian domain. It is part of the intracontinental Atlas chain uplifted by Alpine orogeny (Piqué et al., 2002; Teixell et al., 2003, 2005; Laville et al., 2004).

The WHAM is an extensive metallogenic province containing a variety of base and precious metal deposits and prospects. Some deposits have been exploited since the early 1900s, such as the famous Azegour (Mo, W and Cu), while others are still in production, like Tighardine (Pb-Zn-Cu ± Ag), Amensif (Zn-Cu-Pb ± Ag-Au) and numerous others in development or exploration as well as several artisanal mining sites for barite, iron and base

metals. All these deposits are hosted within the Ediacaran-Palaeozoic basement and are typically located adjacent to major Hercynian granitoids or faults (Ilmen et al., 2015; Boukerrou et al., 2018). In the WHAM, the hydrographic system is dominated by the N'Fis river, originating from the High Atlas. Groundwater resources are highly variable in the Palaeozoic basement, often limited to Quaternary aquifers. Aquifers in the Cretaceous-Eocene strata are well exploitable, while the aquifer in molassic deposits is much more irregular. Despite these numerous discoveries, the massif remains underexplored and undervalued considering its significant natural resources and favourable geological context.

To prospect new sites for mining exploration, we have used satellite data images, which have proved to be a valuable tool in geological mapping and mining exploration (Cetin, 2007; van der Meer et al., 2014; Alshayef & Javed, 2018; Chabane et al., 2019). Indeed, satellite image processing may complement fieldwork in doing inventories of geological lineaments (faults, fractures, etc.), which are favourable zones for fluid flow and consequently subject to hydrothermal alterations leading to significant mineral deposits. On the other hand, geological fractures constitute favourable zones for the infiltration of rainwater towards deep aquifers (fissured aquifer). The use of the satellite data image is particularly beneficial in heavily deformed areas or those with complex deformations, and difficult to access via high altitudes and steep slopes such as our study area. It also an effective tool in developing maps for multiple domains such as urban planning and implementation of large projects such as dams, bridges and roads.

The main objectives of the present study are to use remote sensing and various satellite images (Landsat 8 OLI, Aster and Sentinel 2) in the Tighardine region to: (1) complete the structural mapping of the Tighardine region by extracting geological lineaments and fractures, (2) establish hydrothermal maps, (3) validate remote sensing results by fieldwork data. To achieve this objective, several remote sensing methods accompanied by auxiliary data such as geological and topographic maps and bibliographic data (which will be described in detail in the methods and materials section below), are applied.

2. Geological context

Western High Atlas. The WHAM outcrops comprise Neoproterozoic and Palaeozoic basements composed of multiple basaltic to andesitic lava flows alternating with pyroclastic, volcano-sedimentary and metasedimentary basement overlain by a Meso-Cenozoic cover. During Variscan orogeny, the WHAM basement experienced two main episodes of synshist deformation and low-grade metamorphism (Badra, 1993; Dias et al., 2011). These episodes were accompanied by the intrusion of shallow syn-orogenic to post-orogenic granitoids, as well as the formation of doleritic, lamprophyric and rhyolitic dykes, dated between 347 and 271±3 Ma (Permingeat, 1957; Mabkhout et al., 1988; Gasquet et al., 1992; Loudaoued et al., 2023).

The Meso-Cenozoic cover begins with Triassic deposits. These were subsequently impacted by tectonic activity of faults inherited from the late Hercynian period. These faults, mainly oriented between N20–45°, N70–90° and N120°, control basin geometry. The Triassic extensive tectonic context led to the formation of ENE–WSW to E–W oriented basins in the Tizi n'Test area and throughout the High Atlas. In the coastal zone, these basins trend NNE–SSW, parallel to the Atlantic Rift axis (Qarbous et al., 2003).

During the latest Cretaceous to Oligocene, the convergence between the African and European plates and the closure of the Tethyan Ocean contributed to the Alpine orogeny. The rapprochement of the two plates and their collision generated an intracontinental compression conducting to the closure of the Triassic basins and the formation of the Moroccan Atlas Mountain (Dewey et al., 1989; Ricou, 1994; Missenard et al., 2007). The Atlasic tightening direction varies from NNE–SSW to NNW–SSE between the Maastrichtian-Paleocene and Neogene (Amrhar, 2002; Qarbous et al., 2008; Ibouh & Chafiki, 2017). On the southern side of the WHAM, these Alpine tectonics are expressed by reverse faults generally oriented N70°E, including the western part of the most important Tizi n'Test (TNT) fault accompanied by a network of reverse faults. On the northern side of the WHAM, many left lateral faults trending N70°E to N90°E are responsible for the current structuration. In the northern sub-Atlasic zone, the E–W Medinet fault, which extends over several kilometres, overlaps the Cambro-Ordovician basement on the Meso-Cenozoic cover formations to the west and the metabasites on the Takoucht granodiorite towards Tighardine in the east. The northern limit of the WHAM is represented by the Amezmiz fault whose reactivation, as a reverse fault during the Alpine compression, overlaps the Palaeozoic Azegour block towards the north on the Neogene basin of the Haouz plain (Fig. 1A).

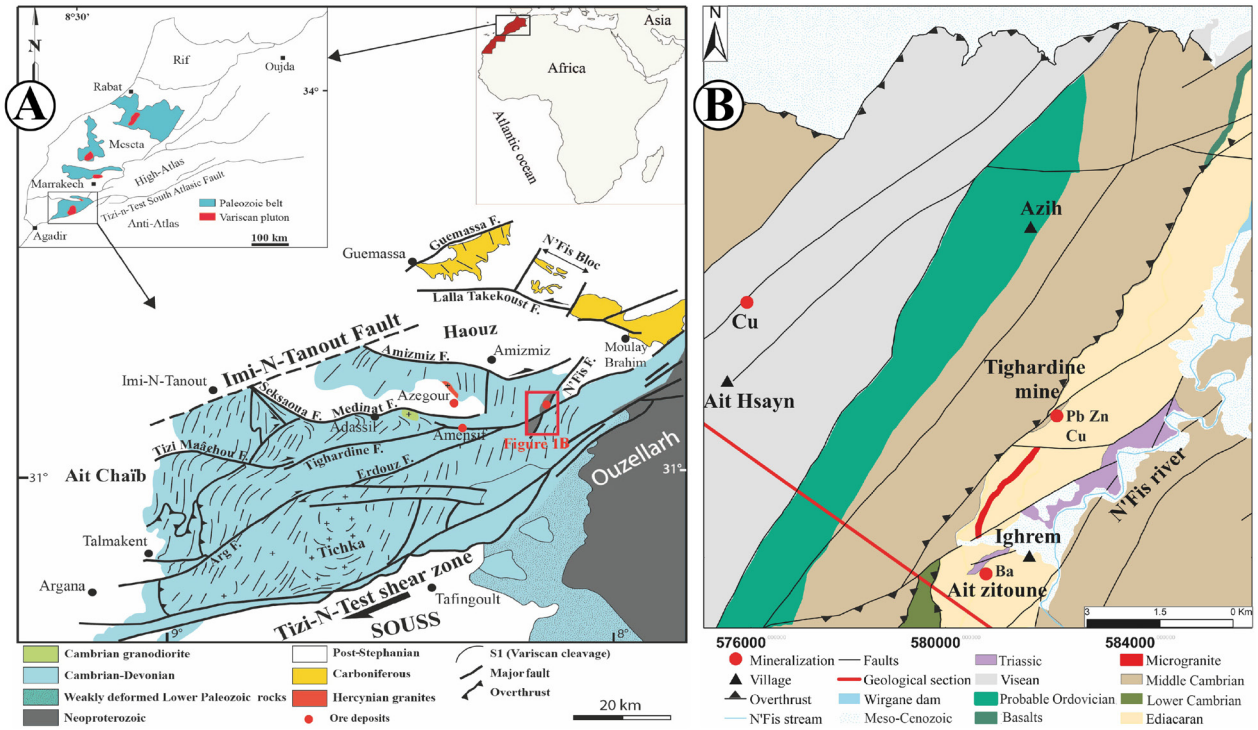

Fig. 1. A – Structural outline of the Western High Atlas of Marrakech. Red rectangle: study area enlarged in Fig. 1B (Dias et al., 2011); **B** – Geological map of the study area (Fekkak et al., 2017).

Tighardine area. The study area chosen for the present work is located on the northern slope of the WHAM, approximately 70 km south of the city of Marrakech. It is bounded by the N'Fis fault to the east, the Medinet fault to the south and the Ait Hsayn fault to the west (Fig. 1B).

The geological formations outcropping in the Tighardine area consist of an upper Neoproterozoic basement represented by the Wirgane granodiorite dated at 625 ± 5 Ma (Eddif et al., 2007), overlain by a volcano-sedimentary series of early Ediacaran age (600 ± 3 Ma) (Boukerrou et al., 2018). This basement sequence is unconformably overlain by a Cambrian shale and sandstone series, followed by Ordovician sandstones and quartzites, and then by Visean shales and sandstones. To the east and south-east of the Tighardine mine, the Triassic red sandstones overlie, in a major unconformity, the Wirgane granodiorite (Fig. 2).

The study area presents a multidirectional fault network, in the direction N–S to NNE–SSW, ENE–WSW to E–W and N140 to N160. The N–S and N70 to N90° directions are shear faults (Fig. 3). They cut the Tighardine Formation into blocks and generally correspond to the contacts with the granodiorite.

The Tighardine Formation recorded low-grade regional metamorphism (greenschist facies) and, locally, low-pressure contact metamorphism which manifests itself, on one side, by the local presence of cordierite and andalusite in the pelitic rocks and on the other hand by the presence of diopside, tremolite and actinolite in dolomitic rocks. These metamorphic minerals are strongly deformed and present sheared zones in some places.

The main mineralised body of the Tighardine polymetallic deposit (Cu, Pb, Zn) has a NE–SW orientation. It has a thickness ranging from 0.5 to 2 m, an average lateral extent of over 1 km, and a depth of 400 m, dipping at 45° to the north-west (Boukerrou et al., 2018). The deposit is located within the Ediacaran volcanic and volcano-sedimentary formations. The main horizon is at the base of the upper dolomite layer and exhibits mineralogical variability as a function of depth, with a predominance of barytes at the top, and massive, banded and brecciated sulphides (Boukerrou et al., 2018).The ore consists mainly of chalcopyrite, sulphoarsenides, galena, sphalerite, bornite, pyrite, arsenopyrite, native silver and magnetite (Alansari et al., 2009; Boukerrou et al., 2018).

3. Materials

The data used in the present study consist of three types of satellite images: Aster, Landsat 8 OLI and Sentinel 2B. They were downloaded free of charge from the United States Geological Survey (USGS)

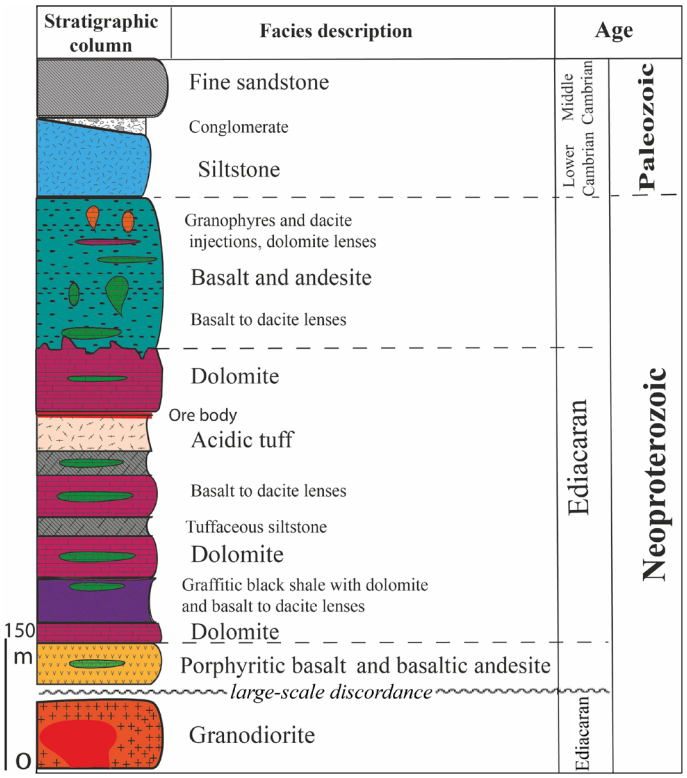

Fig. 2. A synthetic stratigraphical column of the study area (Boukerrou et al., 2018).

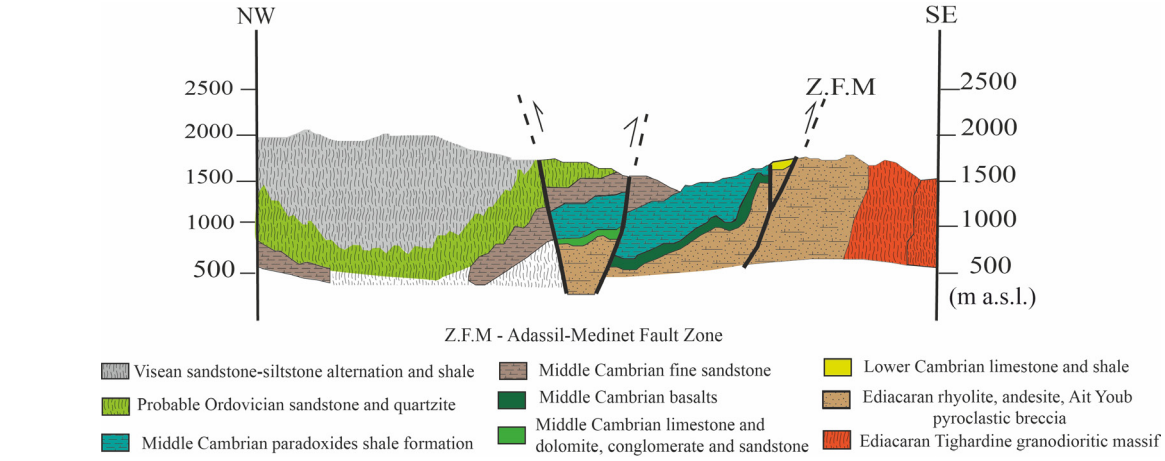

Fig. 3. Structural section extracted from the Amezmiz sheet, redesigned (Ouanaimi et al., 2018).

website and from the website https://scihub.copernicus.eu/. The satellite images were acquired on June 11, 2006, August 14, 2021 and April 16, 2022, respectively.

The Aster satellite image is composed of 14 spectral bands, including three bands in the visible and near-infrared (VNIR) range with a spatial resolution of 15 metres, six bands in the shortwave infrared (SWIR) range with a spatial resolution of 30 metres, and 5 bands in the thermal infrared (TIR) range with a spatial resolution of 90 metres. The Landsat 8 OLI consists of 11 spectral bands, including eight in the visible and infrared range with a spatial resolution of 30 metres, one panchromatic band with a spatial resolution of 15 metres, and two thermal bands with a spatial resolution of 60 metres. Sentinel-2 satellite image has 13 spectral bands, including the visible, near infrared, and short-wave infrared range, with spatial resolutions of 10, 20 or 60 metres, depending on the spectral bands (Table 1).

As auxiliary data, we have used the 1/50,000 geological map of Amezmiz (Ouanaimi et al., 2018) and the 1/100,000 topographic map of Amezmiz. The maps were georeferenced according to the UTM projection, zone 29 north, and the WGS84 datum to match the afore-mentioned satellite images.

Table 1. Spectral bands of data utilised in the present research.

Landsat 8 OLI			Aster			Sentinel 2B		
Band	Wavelenght	Resolution	Band	Wavelenght	Resolution	Band	Wavelenght	Resolution
1	0.43–0.45	30 m	1	0. 52–0. 60	15 m	1	0. 44	60 m
2	0.45–0.51	30 m	2	0. 63–0. 69	15 m	2	0. 49	10 m
3	0.53–0.59	30 m	3N	0. 78–0. 86	15 m	3	0. 56	10 m
4	0.63–0.67	30 m	3B	0. 78–0. 86	15 m	4	0. 66	10 m
5	0.85–0.87	30 m	4	1. 60–1. 70	30 m	5	0. 70	20 m
6	1.56–1.65	30 m	5	2. 15–2. 18	30 m	6	0. 74	20 m
7	2.10–2.29	30 m	6	2. 18–2. 22	30 m	7	0. 78	10 m
8	0.50–0.67	15 m	7	2. 23–2. 28	30 m	8	0. 84	20 m
9	1.36–1.38	30 m	8	2. 29–2. 36	30 m	8A	0. 86	60 m
10	10.60–11.19	30 m	9	2. 36–2. 43	30 m	9	0. 94	60 m
11	11.50–2.51	30 m	10	8. 12–8. 47	90 m	10	1. 37	20 m
			11	8. 47–8. 82	90 m	11	1. 61	20 m
			12	8. 92–9. 27	90 m	12	2. 19	20 m
			13	10.25–10.95	90 m			
			14	10.95–11. 65	90 m			

For a better visual interpretation of the images, pre-processing was necessary, such as radiometric and atmospheric corrections. These corrections were performed using the Fast Line-of-sight Atmospheric Analysis of Spectral Hypercubes (FLAASH) algorithm (Thome et al., 1998) for Aster and Landsat 8 OLI. However, for the Sentinel-2 satellite image, atmospheric correction was carried out using the SNAP application from the Sen2Cor module, resulting in 12 spectral bands with a spatial resolution of 10 metres (https://step.esa.int/main/).

4. Methods

The methodology employed in the present study is based on the satellite image processing to extract geological information in the study area (Fig. 4). For the extraction of faults or fractures in general, indicated by the term "lineament" in remote sensing, we have used principal component analysis and directional filters, and finally, spectral indices have been employed for mapping some alteration minerals that can serve as a mineral prospecting guide.

4.1. Extraction of lineaments

To accentuate and highlight linear structures, which may represent faults, fractures and lithological discontinuities in satellite images, we have made use of directional filters. This process is based on square matrices with different sizes (3×3; 5×5; 7×7) that transform the original image by modifying pixel values based on neighbouring pixel values and utilising special weighting coefficients (Moore & Frederik, 1986; Errami et al., 2023).

For the present work, we have applied filters of size 3×3, 5×5 and 7×7 (Table 1) in four different and main directions N0, N45, N90 and N135 (Table 1)

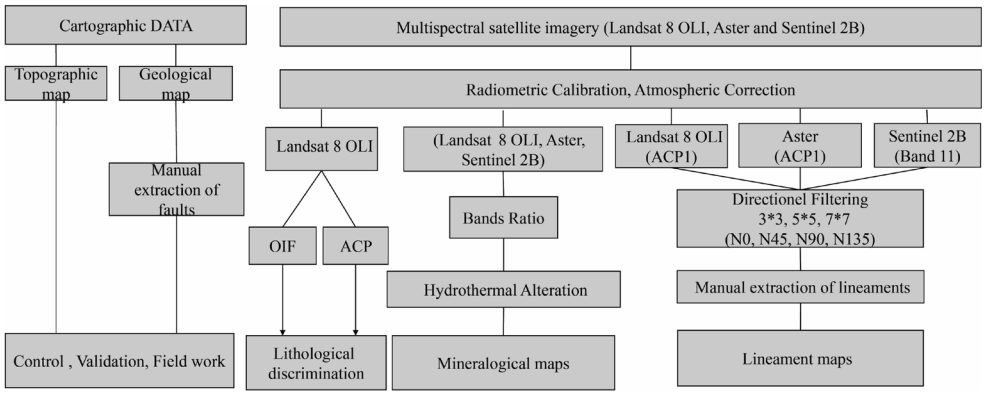

Fig. 4. Flow sheet illustrating the methodology of the different stages used in the present study.

on the ACP1 image for Aster and Landsat 8 OLI and on band 11 of the Sentinel 2B satellite image. The resultant image highlights all linear discontinuities outcropping in the study area (dykes, faults, fractures, lithological discontinuity, etc.). This process enhances the visual perception of linear geological structures on the image (Fig. 5).

The study area lineaments have been carried out manually, by visual analysis of the obtained images from the different filtering steps. Lineament synthetic maps (Fig. 6) have been generated by cataloguing all the linear segments present in the different images (Aster, Landsat 8 OLI, Sentinel 2B) resulting from the filtering process. In order to attribute a geological significance to the lineaments extracted by remote sensing, the lineament maps have been compared with auxiliary data such as geological and topographic maps and field observations. This has allowed to eliminate lineaments related to lithological and topographical (Linear cliff) discontinu-

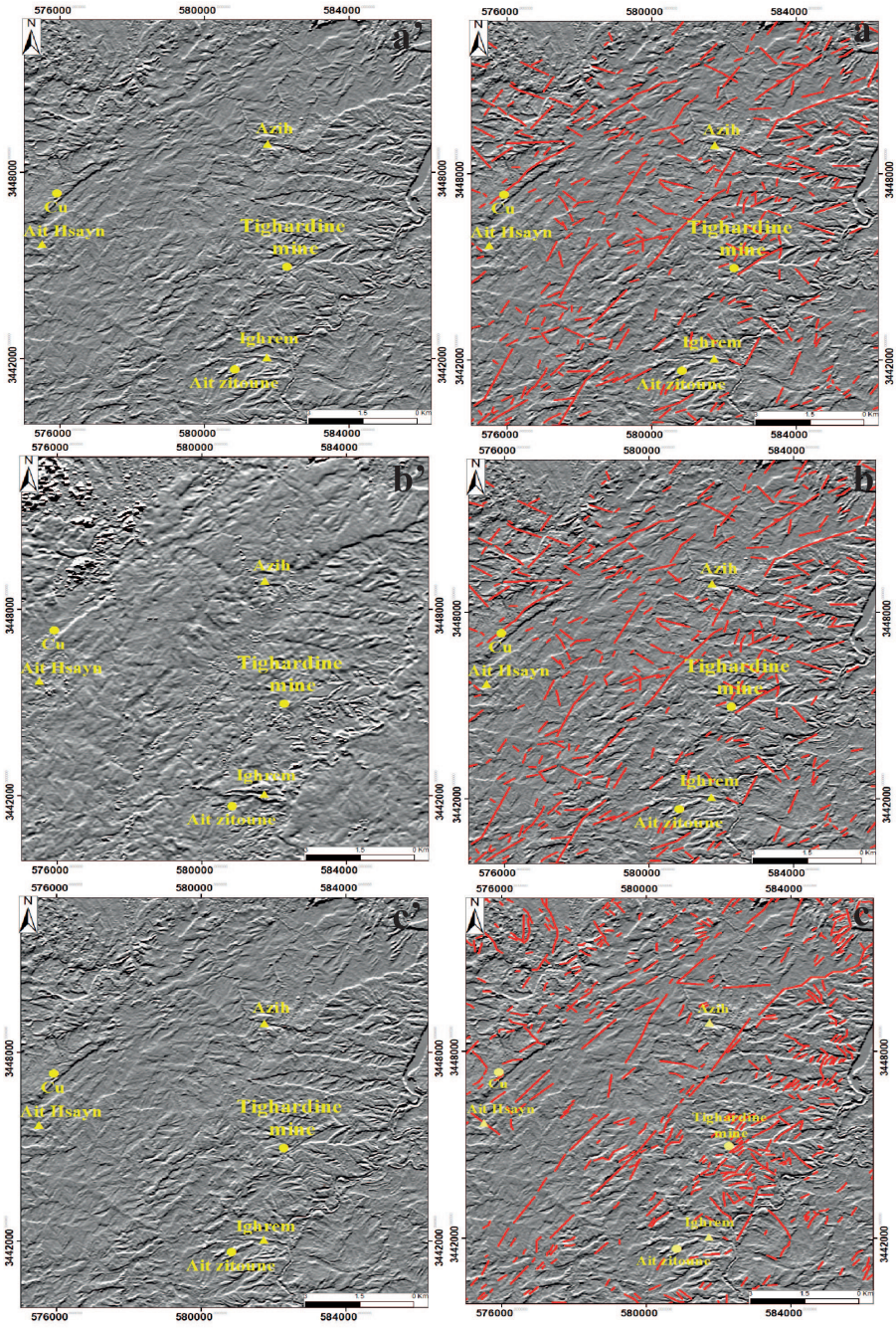

Fig. 5. Resulting image of 5×5 filter for the three types of satellite images: a′, b′, c′ before lineament extraction process; a, b, c with lineaments tracing in red.

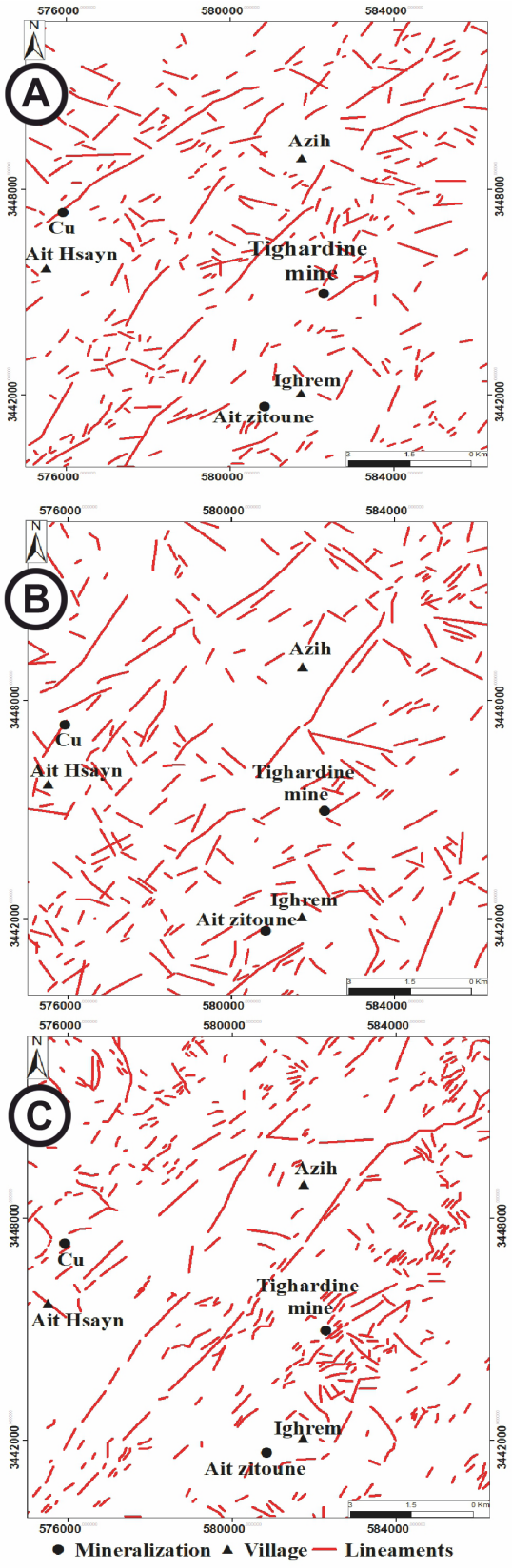

Fig. 6. Synthetic lineament maps obtained from three types of satellite images: **A** – Landsat 8 OLI; **B** – Aster; **C** – Sentinel 2B.

ities and anthropogenic lineaments (paved roads, railways, etc.). The resulting map, after these operations, highlights a significant number of fractures and structural lineaments. Fieldwork has been done in order to validate tectonic lineaments.

4.2. Lithological and mineralogical mapping

The mineralogical mapping is carried out by using two methods: firstly, the Band Ratio (BR) approach for mapping hydrothermal alteration indices in the three types of satellite images (Aster, Landsat 8 OLI and Sentinel 2B). This method is extensively applied in hydrothermal mineral mapping (Pour & Hashim, 2012; Rajendran et al., 2018; Eldosouky, 2019). Specific hydrothermal alteration minerals can be effectively detected using the calculation of absorption and reflection band ratios. The bands are chosen based on the maximum absorption and maximum reflection of the mineral searched for (Inzana et al., 2003; Di Tommaso & Rubinstein, 2007). Generally, VNIR spectral bands are used for identifying iron oxides/hydroxide minerals as they contain crucial information regarding the presence of Fe3+/Fe2+ in the range of 0.45 to 1.2 µm (Hunt & Ashley, 1979). In the present study, we have selected the bands mentioned in Tables 2 and 3. The second method is the Principal Components Analysis (PCA). PCA is a well-known dimension reduction method, which will make it possible to transform highly correlated variables into new variables uncorrelated with each other. In remote sensing, this involves reducing and concentrating most of the information contained in all spectral bands into a certain reduced number of bands. It is a method widely used in various treatments of multispectral satellite images to map lithological units and hydrothermal alteration minerals (Loughlin, 1991; Crósta et al., 2003; Pour & Hashim, 2011, 2012; Chen et al., 2018; Eldosouky, 2019; Zoheir et al., 2019). The PCA transformation allows the mapping of hydrothermal alteration minerals. The analysis of the signs (positive or negative) and the intervals of the eigenvalues makes it possible to detect on the PCA images the zones containing the hydrothermal minerals sought as bright pixels.

Table 2. Some examples of ratios and indices enhancing hydrothermal alteration mineral in Landsat OLI 8 and Sentinel 2B (Kalinowski & Oliver, 2004; Van der Werff & van der Meer, 2016).

Minerals	Landsat OLI	Sentinel 2
Clay minerals	6/7	11/12
Ferrous minerals	5/3+1/2	7/5+3/4
Iron oxide	4/3	4/3

Table 3. Some examples of weathering mineral ratios under Aster images.

Minerals	Ratios	Reference
Alunite, kaolinite, pyrophyllite	(4+6)/5	Gozzard (2006)
Ferric iron, Fe3+	(2/4)	Rowan et al. (2003)
Ferrous iron, Fe2+	5/3 + 1/2	Rowan et al. (2006)
Silica	(11x11)/10/12	Bierwith (2002)
Dolomite	(6+8)/7	Gozzard (2006)

The raw bands to be transformed by PCA are those where the mineral shows maximum absorption and that where it shows maximum reflection (Loughlin, 1991; Cŕosta et al., 2003).

The lithological map is produced by satellite image processing which allows an increase in visual discrimination of facies. Two processing images are used, Principal Component Analysis (PCA) largely described above and the Optimum Index Factor (OIF). The OIF is a statistical value that can be used to select the optimal combination of three bands to make an optimal coloured composite of a satellite image. The optimal combination of bands among all possible 3-band combinations is the one that contains the greatest amount of different information with the least repetition. It is calculated by a ratio of the standard deviations Sum, of the different three-band combinations, to the Sum of the correlation coefficient absolute values. The combination with the highest OIF is likely to provide the maximum lithological information (Qaid & Basavarajappa, 2008; Berraki et al., 2012; El Atillah et al., 2018; El Janati, 2019) (see Table 4).

Table 4. Result of optimal index factor calculation (OIF).

Coloured compound	Red channel	Green channel	Blue channel	OIF
1	Band 5	Band 6	Band 7	9611.49
2	Band 4	Band 5	Band 6	9061.19
3	Band4	Band 6	Band 7	8923.38
4	Band 3	Band 5	Band 6	8649.54
5	Band 4	Band 5	Band 7	8578.37
6	Band 1	Band 5	Band 6	8570.79

4.3. Fieldwork

In order to validate and verify the information and data extracted by remote sensing on the different satellite images used, we have identified zones of hydrothermal alteration on the images derived by processing with sampling of geographic co-ordinates. Subsequently, a field campaign was organised to verify, on the one hand, the accuracy of the results in the field. On the other hand, this was done so as to collect samples for thin sections and microscopic investigations to examine the mineral alterations identified by remote sensing. The field missions will also make it possible to quantify the orientations of geological structures and the extent of hydrothermal zones detected on the images.

5. Results and discussion

5.1. Lineaments mapping

The resultant lineament synthetic maps reveal 447 lineaments from Landsat 8 OLI image, 394 from ASTER and 743 from Sentinel 2B. Lineaments present different shapes and sizes (Fig. 6). The analysis of the three lineaments maps shows three main fractures sets in the three satellite images cited above. The main and major fracture sets, extracted and common in the three types of images, are NE–SW and NW–SE. A third fractures set oriented E–W is minor (Fig. 7A, B, D; Table 5).

The lineament maps (especially those obtained from Landsat 8 OLI and Sentinel 2B images) confirm the fault sets oriented NE–SW indicated on the geological map of Amezmiz 1/50.000 (Fekkak et al., 2017) (Fig. 8B).The lineaments allow also mapping new faults oriented E–W and NW–SE. The mapping of major faults only on the geological map (Fekkak et al., 2017) may explain the disparity between the results of remote sensing and the geological map.

Comparing the directions of lineaments obtained from remote sensing with existing geological studies by Boukerrou et al. (2018), a significant correlation is observed. Also, according to our field observations, the Tighardine region is affected by numerous faults with varied orientations, ranging from N–S to NNE–SSW, ENE–WSW to E–W and N140 to N160. However, faults oriented from N50° to N70° and E–W are relatively abundant in the study area (Taib et al., 2020). These orientation sets confirm those extracted by remote sensing in this work. Additionally, the directions found by remote sensing are compatible with the directions of the great Medinet fault, oriented N90° to N120°, as well as the N'Fis fault, oriented N10°E to N20°E. Furthermore, the Taourirte-Tighardine fault is parallel to the N'Fis fault, and other similar examples were described by Taib et al.(2020).

The ENE–WSW to ESE–WNW and SSE–NNW directions are weakly detected by remote sensing.

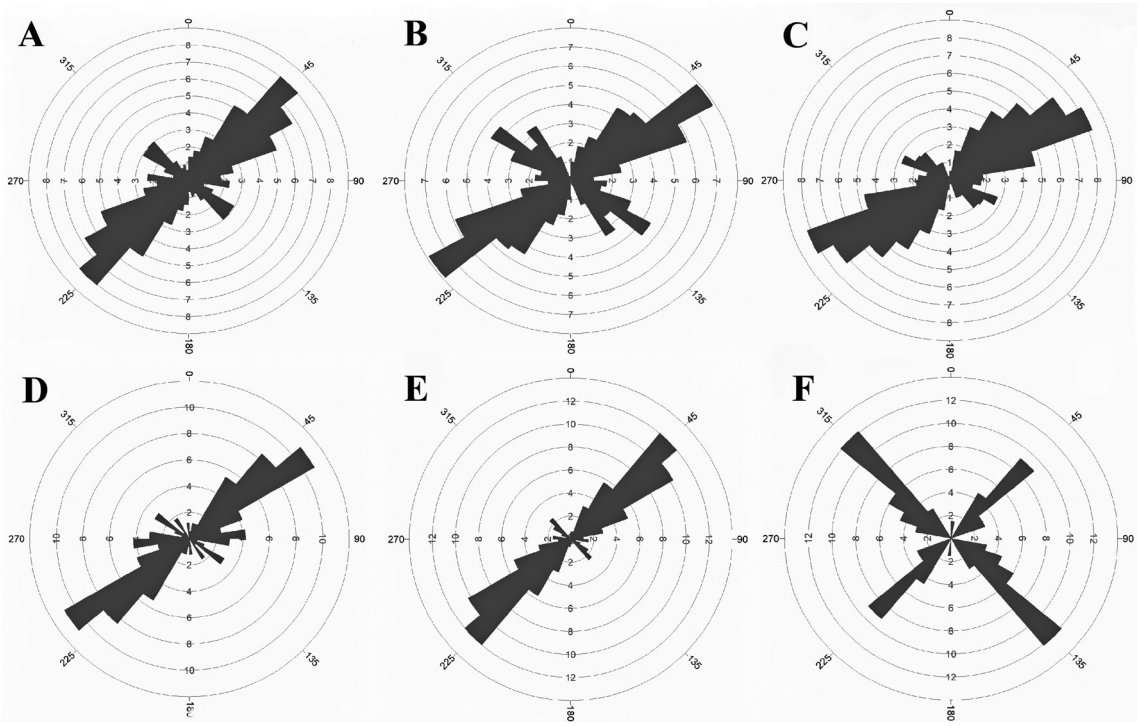

Fig. 7. Rose diagrams of lineaments extracted from satellites images: **A –** Sentinel 2B; **B –** Aster; **C –** Landsat 8 OLI. Rose diagrams of lineaments extracted from Sentinel 2B for geological formations of different ages: **D –** Ediacaran; **E –** Palaeozoic; **F –** Meso-Cenozoic.

Table 5. Number and frequency of three set faults extracted from satellites images used in the present work.

Direction	Landsat 8 Oli		Aster		Sentinel 2B	
	Number of faults	Frequency (%)	Number of faults	Frequency (%)	Number of faults	Frequency (%)
NE–SW	370	75.66	240	62.18	614	82.64
NW–SE	94	19.22	126	32.64	93	12.52
E–W	25	5.11	20	5.18	36	4.85

They correspond to secondary faults resulting from successive tectonic activities during the Hercynian and Atlasic orogenesis (Taib et al., 2020).

To validate the lineament map obtained by remote sensing, field measurements were conducted. The diagram rose (Fig. 8A) reveals the presence of two main directions: NE–SW and E–W. The E–W orientations are highly prevalent in the field measurements but appear less frequently in the directional roses diagram derived from remote sensing lineaments. This suggests that these two lineaments sets crop out at the local scale of Tighardine and expressed specifically in the Ediacaran basement, but are less extensive on a global scale. The same observation is valid for N–S oriented faults.

In order to evaluate the role of various orogenesis (Pan-African, Hercynian and Atlasic) and to examine the relationship between the lithological nature and ages, the orientation and density of lineaments, we have divided the study area depending on ages of formations so as to detect outcropping frequency and trends of lineaments using Sentinel 2Bimage. The analysis of relationship cited above reveals that:

- The Ediacaran outcrops show 120 lineaments oriented NE–SW, representing 70 per cent of the total and the E–W direction represent 24.74 per cent. These two fault sets are probably inherited from the late Pan-African deformations and were reactivated during Hercynian and Alpine tectonic episodes. Such directions coincide with the well-known Tizi n'Test fault, oriented N70°E to E–W and worked in dextral shear during Hercynian deformations (Dias et al., 2011).
- The Palaeozoic outcrops display 317 lineaments mainly oriented NE–SW. This trend, already described in the Ediacaran formations, is linked to the N70°E shear zones and granitic intrusions attributed to the late stage of Palaeozoic extension by Badra et al. (1991).

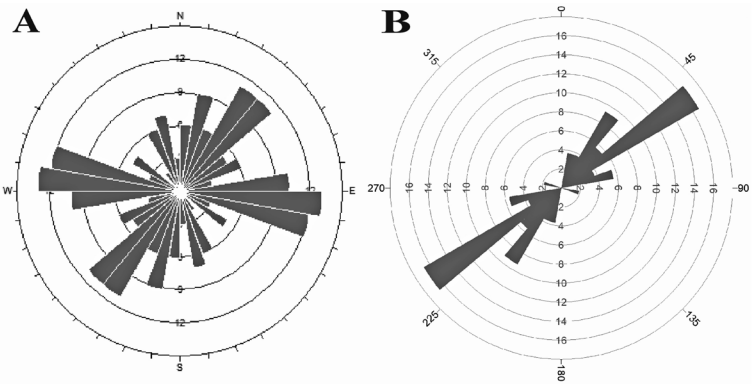

Fig. 8. A –Rose diagrams representing faults observed in the field (locally at Tighardine area); **B** – Faults extracted from the Amezmiz geological map (Fekkak et al., 2017).

– The Meso-Cenozoic outcrops exhibit 48 lineaments, and the main direction is NW–SE. This trend expresses the tectonic impact of Mesozoic events in our region. The NW–SE faults were activated as normal during Triassic rifting and reactivated in reverse during Alpine compression (Badra et al., 1991; Dias et al., 2011; Fekkak et al., 2018).

In terms of regional tectonics, the rose diagram obtained based on geological ages validates the known fault trends in the region, confirming the impact of tectonic events in the Tighardine area.

5.2. Lineament density

Lineament density is an important parameter widely used in lineament characterisation (Lachaine, 1999; Corgne et al., 2010; Hashim et al., 2013). The production and analysis of lineament density maps allow us to assess the lineament concentration in relation to the different outcrops (Lachaine, 1999). Fracture density maps highlight high concentrations in the Ediacaran basement outcrops (especially in the Sentinel 2B and Landsat 8 OLI images), which is a heavily deformed area in the Amezmiz zone during the Variscan compression (Ouanaimi et al., 2018). They are also aligned along the major NE–SW-oriented geological faults in the study area (Fig. 9).

We have noted that the fractures extracted by remote sensing are more numerous and denser than those identified on the Amezmiz geological map (1/50,000). This could be attributed to the fact that only large extension faults have been mapped on the geological map, as already mentioned above.

5.3. Analysis of lineament lengths

The analysis of lineament lengths reveals a range of variation from 6.6 metres to 1.07 kilometres for the Sentinel image, from 56.9 metres to 1.6 kilometres for Landsat 8 OLI, and from 6.4 metres to 1.16 kilometres for Aster (Fig. 10). However, the majority of lineament lengths extracted from the three types of images varies 0.1 and to 0.4 kilometres, while lineaments longer than 1 kilometre are infrequent and represent approximately 4 per cent in the map lineament derived from Aster image.

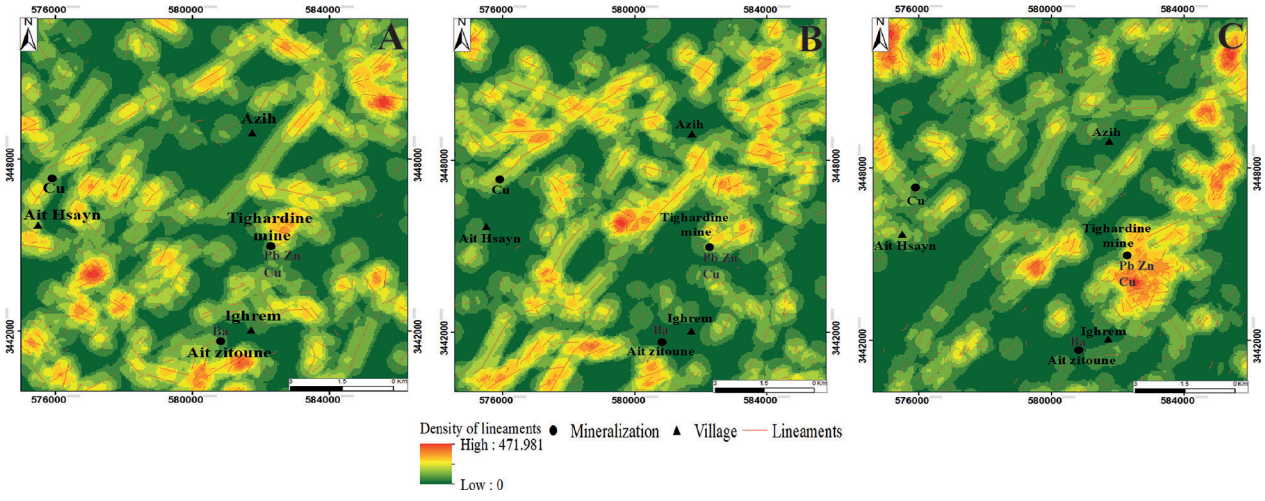

Fig. 9. Density maps extracted by remote sensing: **A** – Aster image; **B** – Landsat 8 OLI image; **C** – Sentinel 2B image.

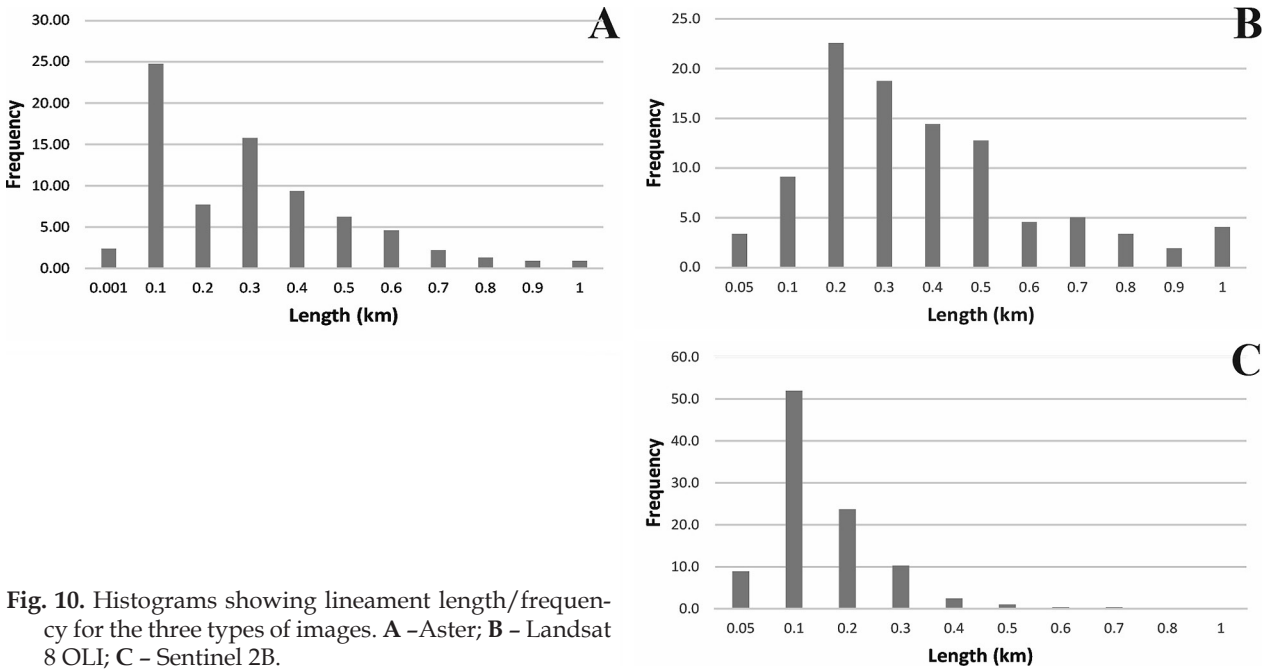

Fig. 10. Histograms showing lineament length/frequency for the three types of images. **A** –Aster; **B** – Landsat 8 OLI; **C** – Sentinel 2B.

5.4. Lithological mapping

The lithological map extracted from coloured composite PCA1, PCA2 and PCA3 has allowed us to delineate various geological formations in the study area (Fig. 11A). The Ediacaran basement is depicted in a purple shade, middle Cambrian fine sandstones in sky blue and Visean schists, predominantly observed in the south-west of the study area, is highlighted in yellow. In the northern part, where Cenozoic formations appear, particularly Paleogene and Quaternary, it is challenging to differentiate them;

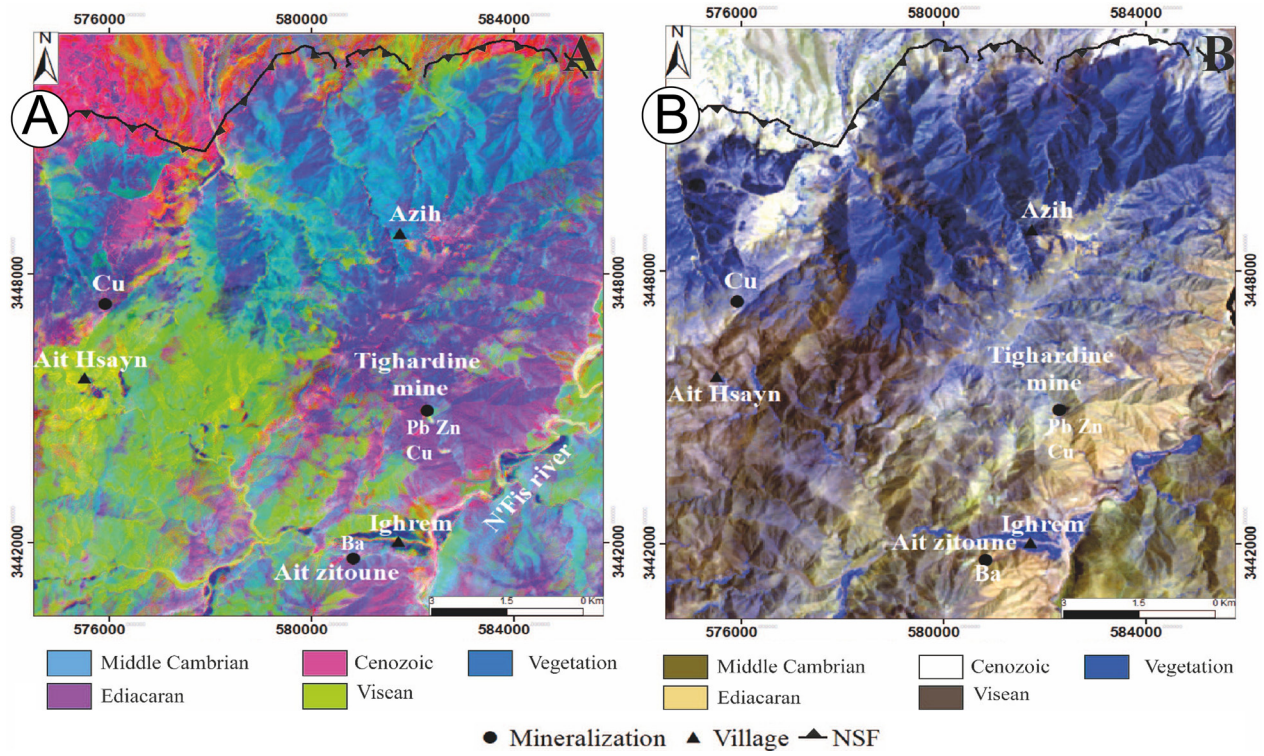

Fig. 11. Colour composite from: **A** – Principal Component Analysis (PCA_{123}); **B** – Uncorrelated bands 5, 6 and 7 of the OIF method.

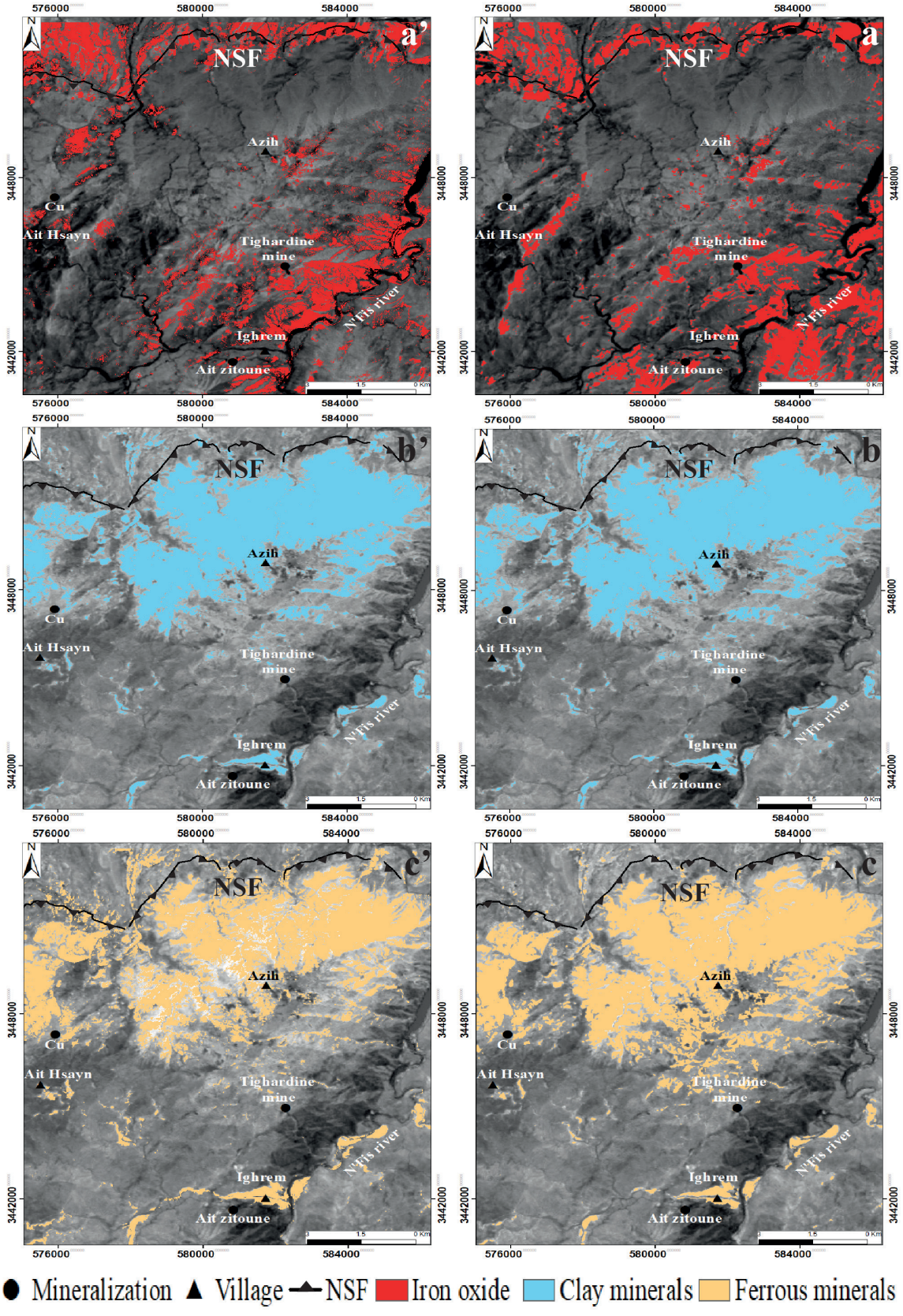

Fig. 12. Map of spectral indices (clay minerals in blue, iron oxide in red, ferrous minerals in beige) extracted from the Sentinel 2B (a', b', c') and Landsat 8 OLI (a, b, c). NSF - northern subatlasic fault.

they are represented by orange and pink hues, respectively. Heavily vegetated regions are displayed in blue (Fig. 11A).

The coloured composite of bands 5, 6 and7 with the highest OIF has validated the lithological units previously identified by the PCA. However, there are notable differences. The OIF method distinctly identifies the Ediacaran formation through a light beige hue (Fig. 11B), the fine green sandstones of the Middle Cambrian represented by a pistachio colour, and the Visean schist formations by brown. Nevertheless, this method does not separate Paleogene and Quaternary formations, possibly due to the lithological similarity of their facies. Dense vegetation areas are also indicated in blue (Fig. 11B).

Among the differences observed between the obtained maps (Fig. 11A, B) and the geological map (Fig. 1B) is that the formation considered to be Ordovician in age is represented by the same colour as the Visean and Quaternary depositions overlying the Cambrian formations in the NNW part of the study area.

5.5. Mineralogical mapping

Analysis of results from processing indices using Landsat 8 OLI and Sentinel 2B imagery enables the identification of mineral distribution within the study area (Fig. 12). Clay minerals are localised primarily in the river, which is likely due to water drainage during floods, and they settle in low-lying topographical areas. Therefore, the clay minerals found in the river may not necessarily result from significant clay alteration in the Cambrian pelitic formations. The localised presence of this band may be related to lithological variations, specifically the abundance of sericite-shale in the Cambrian pelitic formations as shown by petrographic observations.

Ferrous minerals are located in the same areas as clay minerals, indicating that the same phenomenon controls both types of alteration. Iron oxides are arranged along oxidation corridors oriented along the major NE–SW structures, which correspond to the orientation of the mineralised horizon in the study area (magnetite, hematite, etc.) and the overlapping zone associated with the northern sub-Atlasic fault (NSF) (Ouanaimi et al., 2018) that delimits the studied northern block. They are also present in the Ediacaran basement. As for ferrous minerals, they are localised mainly in the central part of the altered Middle Cambrian basaltic formations and in the eastern part of the clay alteration zone.

In conclusion, processing of the Sentinel 2B and Landsat 8 OLI satellite images displays the same alterations in the same places for the three types of alteration indices (clay minerals, iron oxide and ferrous minerals) (Fig. 12).

The spatial maps of hydrothermal alteration minerals derived from processing Aster images, such as silica, dolomite, carbonate, ferrous minerals and iron oxide, were plotted on the same map allowing observation of the spatial relationship between the various detected anomalies (Fig. 13).

The results shown in Figure 13 exhibit some similarity to the index maps extracted from Landsat OLI and Sentinel 2B images. The iron oxides are located along the fault defining the northern boundary of the study area and within the Ediacaran formations. Silica appears in an outcrop area corresponding to the Ediacaran basement, which hosts the mineralised zone. Moreover, the ferrous minerals are localised primarily in the northern part of the study area, mainly within the alternating sandstone-shale formations of the Visean and in the Upper Cretaceous red clay formations. They may also be associated with altered tuffs and basalts occurring in the Middle Cambrian (Ouanaimi et al., 2018).

Indeed, fieldwork and thin section observation have shown that the study area is characterised by an abundance of silicification phenomena within dolomites (silicified dolomitic lenses) and an abun-

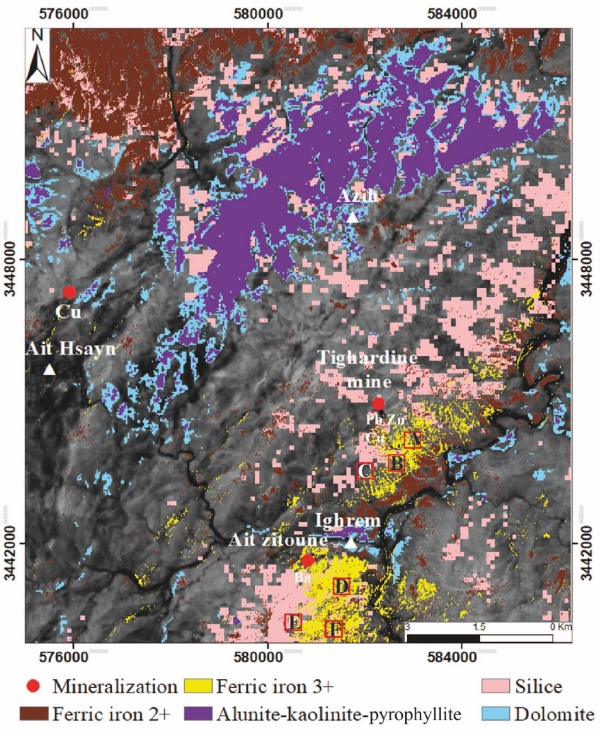

Fig. 13. Map displaying all spectral indices extracted from Aster image; A, B, C, D, E, F – locations of images in Figure 14.

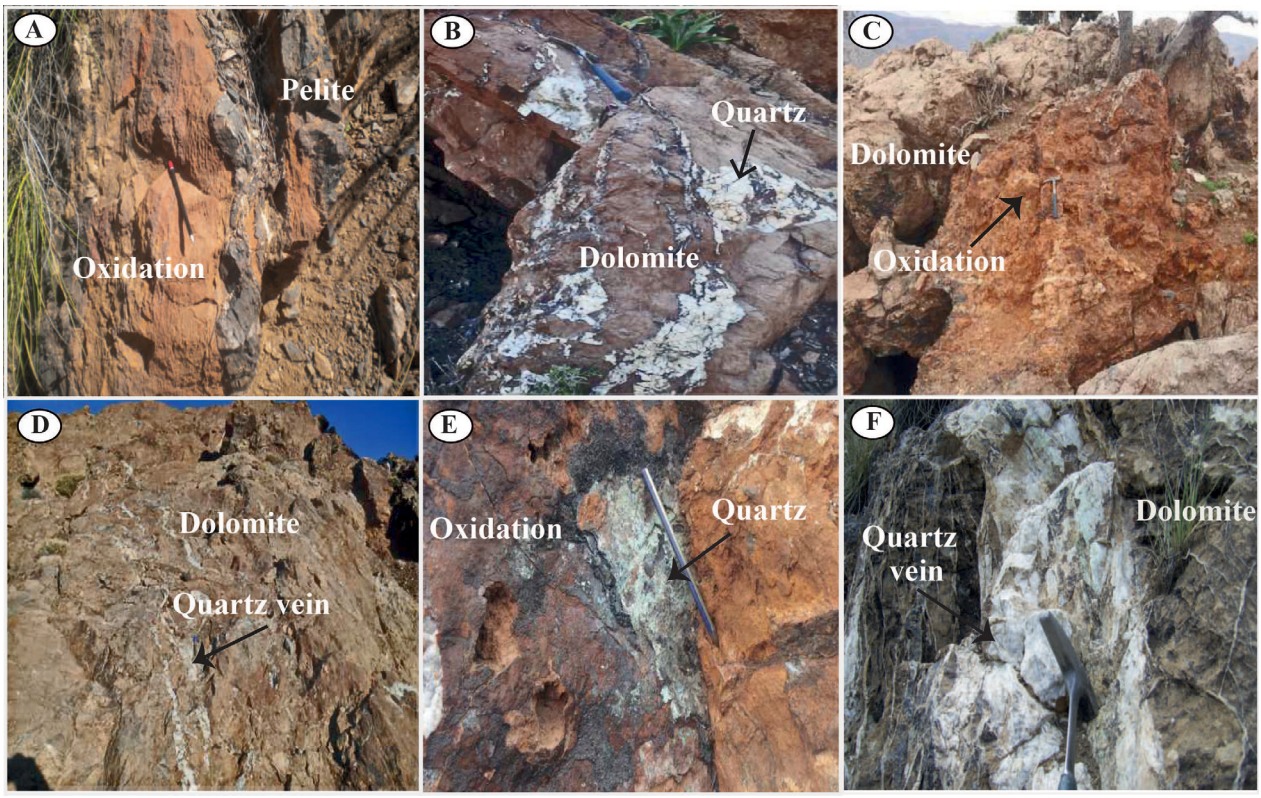

Fig. 14. Field photographs showing alterations. **B, D, F** – dolomites affected by quartz veins. **C** – Heavily weathered dolomites with old artisanal mining galleries. **A, E** – ferric alteration.

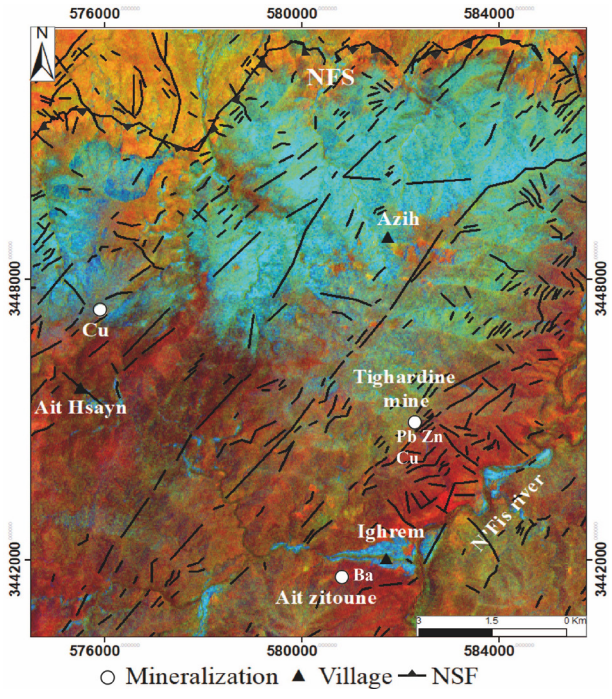

Fig. 15. RGB colour composite of band ratios 2/1, 4+6/5, and 3/2 (areas of hydrothermal alteration represented by dark orange pixels) with extracted lineaments from Sentinel 2B image.

dant presence of silicified veins and fractures (Figs. 14, 16).

The RGB colour composition of the 2/1, 4+6/5, and 3/2 band ratios (Fig. 15) has revealed areas of hydrothermal alteration by dark orange pixels. These zones correspond perfectly to the hydrothermal alteration areas obtained by remote sensing (Figs. 12, 13), which are in agreement with the mineralised zone and the faults crossing the region (NSF in the northern part of the study area).

6. Conclusions

The present study discusses the integration of multispectral data from ASTER, Landsat 8 OLI and Sentinel 2B sensors for the mapping of lineaments (geological fractures) and hydrothermal alteration minerals associated with the mapping of fractures in the Tighardine area (Western High Atlas of Marrakesh). Fracture mapping was carried out using Landsat 8 OLI, ASTER and Sentinel 2 satellite image processing. This analytical technique allows to identify networks of lineaments that affected the study area. Results obtained indicate that these lineaments are divided into three major sets of direc-

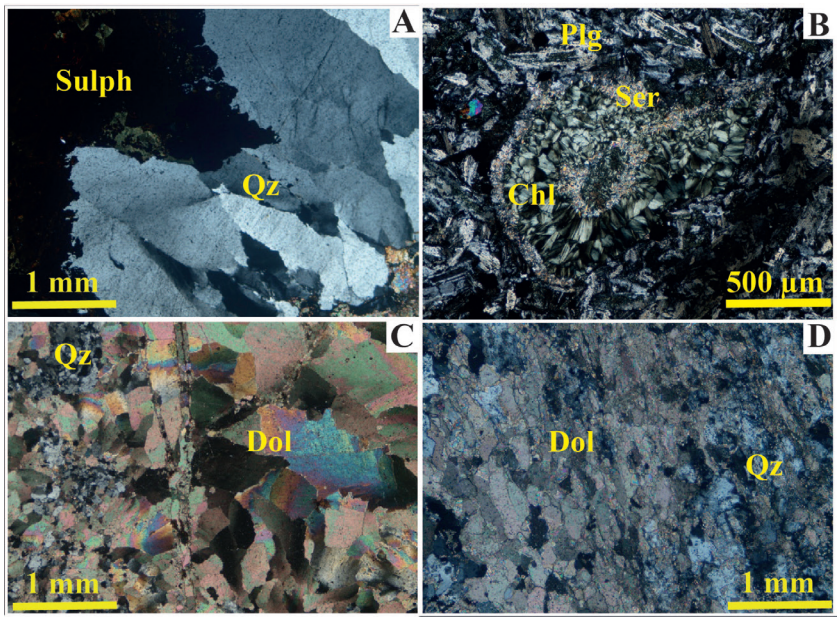

Fig. 16. Microscopic photographs of hydrothermal alteration minerals. Cross-polarised light. **A** – Silicification associated with sulphide; **B** – Agglomeration of chlorite minerals surrounded by sericite within basalt; **C, D** – Silicified dolomites. Qz – quartz, Dol –dolomite, Ser – sericite, Sulph – sulphide, Plg – plagioclase, Chl – chlorite.

tions. The main one is NE–SW, which is the most frequent and longest (with a percentage of 75.66 per cent for Landsat 8 OLI, 62.18 per cent for ASTER, and 82.54 per cent for Sentinel 2). This direction is the best known in the study area. The two new fracture sets identified by remote sensing are NW–SE (moderately represented on lineament maps), represented in Mesozoic-Cenozoic formations, and E–W (the least represented on lineament maps), occurring in outcrops of Ediacaran basement.

Landsat 8 OLI, Sentinel 2 and ASTER satellite images have also been used to establish hydrothermal alteration mineral maps in the study area. The map analysis has revealed two potential target areas: in the south-east of the study area the Neoproterozoic basement displays alterations of silica, dolomite, iron minerals, clay minerals, iron oxide and alunite-kaolinite-pyrophyllite. These alteration zones are oriented along the major NE–SW structures corresponding to the orientation of the mineralised horizon of the Tighardine ore deposit. Results obtained hint at an extension of this horizon towards the south-west at the Ait Zitoune and towards the west in the Ait Hsayn region. The second area is situated in the northern part, at the Cambrian-Cenozoic boundary, where the most abundant alterations are carbonation, silicification and iron (Fe^{2+}) oxidation, covering extensive areas.

Acknowledgements

This work is part of the PhD thesis of the senior author, supported by the European project (Project 101086250 — EWALD — HORIZON-MSCA-2021-SE-01). We thank the journal editor for valuable comments and two anonymous reviewers for their comments and suggestions, which contributed to improving the content of this paper.

References

Alansari, A., Bajddi, A. & Zouhair, M., 2009. Mise en évidence d'une évolution verticale dans la minéralogie et la typologie des minéralisatios à CU-Zn-Pb-Ag-Ba de Tighardine: Apports à l'exploration minière dans le Haut Atlas occidental (Maroc) [Highlighting a vertical evolution in the mineralogy and typology of CU-Zn-Pb-Ag-Ba mineralizations of Tighardine: Contributions to mining exploration in the Western High Atlas (Morocco)]. *Notes Mémoire du Service Géologique du Maroc* 530, 31–44.

Alshayef, M.S. & Javed, A., 2018. Geomatica-Based Approach for Automatic Extraction of Lineaments from ASTER-GDEM Data, in Part of Al-Rawdah, Shabwah, Southeast Yemen. 423–434, https://doi.org/10.1007/978-981-10-5801-1_29

Amrhar, M., 2002. Paléocontraintes et déformations syn- et post-collision Afrique-Europe identifiées dans la couverture mésozoïque et cénozoïque du Haut Atlas occidental (Maroc) [Syn- and post-Africa-Europe collision paleostresses and deformations identified in the Mesozoic and Cenozoic cover of the Western High Atlas (Morocco)]. *Comptes Rendus Geoscience* 334, 279–285, https://doi.org/10.1016/S1631-0713(02)01730-3

Badra, L., 1993. *Les minéralisations polymétalliques (Pb, Zn, Cu, Ba) du Haut-Atlas occidental Marocain et de ses confins dans leur cadre géodynamique*. Université d'Orléans, France, 415 pp.

Badra, L., Prost, A.E., & Touray, J.C., 1991. Chronologie relative des minéralisations Zn-Pb de la région de l'Erdouz (district d'Azegour) et des phases de déformation hercyniennes dans le Haut-Atlas occidental plissé (Maroc) [Relative chronology of Zn-Pb miner-

alization in the Erdouz region (Azegour district) and Hercynian deformation phases in the folded Western High Atlas (Morocco)]. *Comptes rendus de l'Académie des Sciences. Série 2* 313, 331–337.

Berraki, F., Bendaoud, A., Brahimi, B. & Djemai, S., 2012. Cartographie et étude pétrographique et minéralogique des dykes de dolérites de l'in ouzzal (Hoggar occidental, Algérie) [Mapping and petrographical and mineralogical study of the dolerite dikes of l'in ouzzal (Western Hoggar, Algeria)]. *Photo-Interprétation European. Journal of Applied Remote Sensing* 1–2, 533–535.

Boukerrou, S., Nalini, H., Moreira, H., Maacha, L., Zouhair, M., Outhounjite, M., Ouirouane, S., Hibti, M. & Touil, A., 2018. Geochronology and geochemistry of Ediacaran volcanic rocks of the Tighardine ore deposit formation (western High Atlas, Morocco). *Arabian Journal of Geosciences* 11, 22. https://doi.org/10.1007/s12517-017-3375-4

Cetin, K.S.K., 2007. A detailed geologic lineament analysis using Landsat TM data of Gölmarmara Manisa Region, Turkey. *Earth Sciences* 1, 145–153.

Chabane, S., Amri, K. & Hamdidouche, R., 2019. Deformation pattern in the El Ahmar area (Bechar Basin, Southwestern Algeria): contribution of Lansat 8 OLI and field measurement. *Arabian Journal of Geosciences* 12, 158. https://doi.org/10.1007/s12517-019-4311-6

Chen, G., Li, S., Knibbs, L.D., Hamm, N.A.S., Cao, W., Li, T., Guo, J., Ren, H., Abramson, M.J. & Guo, Y., 2018. A machine learning method to estimate PM2.5 concentrations across China with remote sensing, meteorological and land use information. *Science of the Total Environment* 636, 52–60. https://doi.org/10.1016/j.scitotenv.2018.04.251

Corgne, S., Magagi, R., Yergeau, M. & Sylla, D., 2010. An integrated approach to hydro-geological lineament mapping of a semi-arid region of West Africa using Radarsat-1 and GIS. *Remote Sensing of Environment* 114, 1863–1875. https://doi.org/10.1016/j.rse.2010.03.004

Cŕosta, A.P., De Souza Filho, C.R., Azevedo, F. & Brodie, C., 2003. Targeting key alteration minerals in epithermal deposits in Patagonia, Argentina, using ASTER imagery and principal component analysis. *International Journal of Remote Sensing* 24, 4233–4240. https://doi.org/10.1016/j.rse.2010.03.004

Dewey, J.F., Helman, M.L., Knott, S.D., Turco, E. & Hutton, D.H.W., 1989. Kinematics of the western Mediterranean. *Geological Society Special Publication* 45, 265–283. https://doi.org/10.1144/GSL.SP.1989.045.01.15

Dias, R., Hadani, M., Leal Machado, I., Adnane, N., Hendaq, Y., Madih, K. & Matos, C., 2011. Variscan structural evolution of the western High Atlas and the Haouz plain (Morocco). *Journal of African Earth Sciences* 61, 331–342. https://doi.org/10.1016/j.jafrearsci.2011.07.002

Di Tommaso, I. & Rubinstein, N., 2007. Hydrothermal alteration mapping using ASTER data in the Infiernillo porphyry deposit, Argentina. *Ore Geology Reviews* 32, 275–290. https://doi.org/10.1016/j.oregeorev.2006.05.004

Eddif, A., Gasquet, D., Hoepffner, C. & Levresse, G., 2007. Age of the Wirgane granodiorite intrusions (Western High-Atlas, Morocco): New U-Pb constraints. *Journal of African Earth Sciences* 47, 227–231.

El Atillah, A., El Morjani, Z.E.A. & Souhassou, M., 2018. Utilisation de l'image multispectrale pour l'exploration et la recherche des ressources minérales : État des connaissances et proposition d'un modèle de traitement [Use of multispectral images for exploration and research of mineral resources: State of knowledge and proposal of a processing model]. *European Scientific Journal* 14, 350. https://doi.org/10.19044/esj.2018.v14n24p350

El Janati, M., 2019. Application of remotely sensed ASTER data in detecting alteration hosting Cu, Ag and Au bearing mineralized zones in Taghdout area, Central Anti-Atlas of Morocco. *Journal of African Earth Sciences* 151, 95–106. https://doi.org/10.1016/j.jafrearsci.2018.12.002

Eldosouky, A.M., 2019. Aeromagnetic data for mapping geologic contacts at Samr El-Qaa area, North Eastern Desert, Egypt. *Arabian Journal of Geosciences* 12, 2. https://doi.org/10.1007/s12517-018-4182-2

Errami, M., Algouti, A., Algouti, A., Farah, A. & Agli, S., 2023. Utilization of ASTER data in lithological and lineament mapping of the southern flank of the Central High Atlas in Morocco. *Geologos* 29, 1–20. https://doi.org/10.14746/logos.2023.29.1.01

Fekkak, A., Ouanaimi, E.M., Ettachfini, H., El Arabi, H., Jouhari, A., Aarab, A. &, Baidder, L., 2017. *Carte géologique du Maroc au 1/50, 000*.

Fekkak, A., Ouanaimi, H., Michard, A., Soulaimani, A., Ettachfini, E.M., Berrada, I., El Arabi, H., Lagnaoui, A. & Saddiqi, O., 2018. Thick-skinned tectonics in a Late Cretaceous-Neogene intracontinental belt (High Atlas Mountains, Morocco): The flat-ramp fault control on basement shortening and cover folding. *Journal of African Earth Sciences* 140, 169–188. https://doi.org/10.1016/j.jafrearsci.2018.01.008

Gasquet, D., Leterrier, J., Mrini, Z. & Vidal, P., 1992. Petrogenesis of the Hercynian Tichka plutonic complex (Western High Atlas, Morocco): Trace element and RbSr and SmNd isotopic constraints. *Earth and Planetary Science Letters* 108, 29–44. https://doi.org/10.1016/0012-821X(92)90058-4

Hashim, M., Ahmad, S., Johari, M.A.M. & Pour, A.B., 2013. Automatic lineament extraction in a heavily vegetated region using Landsat Enhanced Thematic Mapper (ETM+) imagery. *Advances in Space Research* 51, 874–890. https://doi.org/10.1016/j.asr.2012.10.004

Hunt, G.R. & Ashley, R.P., 1979 . Spectra of altered rocks in the visible and near infrared. *Economic Geology* 74, 1613–1629.

Ibouh, H & Chafiki, D., 2017. Le Maroc, paradis des géologues [Morocco, paradise for geologists]. *Societe Geologique de France* 194, 3–126.

Ilmen, S., Alansari, A., Baidada, B., Maacha, L. & Bajddi, A., 2015. Minerals of the Ag-Bi-Cu-Pb-S system from the Amensif carbonate-replacement deposit (western High Atlas, Morocco). *Journal of Geochemical Exploration* 161, 85–97. https://doi.org/10.1016/j.gexplo.2015.11.008

Inzana, J., Kusky, T., Higgs, G. & Tucker, R., 2003. Supervised classifications of Landsat TM band ratio images and Landsat TM band ratio image with radar for geological interpretations of central Madagascar. *Journal of African Earth Sciences* 37, 59–72. https://doi.org/10.1016/S0899-5362(03)00071-X

Kalinowski, A. & Oliver, S., 2004. Aster Mineral Index Processing Manual. *Remote Sensing Applications Geoscience Australia. Comparative Biochemistry and Physiology – Part A: Physiology* 53, 123–127, https://doi.org/10.1016/S0300-9629(76)80023-0

Lachaine, G., 1999. *Structures géologiques et linéaments Beauce, (Québec) : apport de la télédétection*. Image, Rochester, USA, 105 pp.

Laville, E., Pique, A., Amrhar, M. & Charroud, M., 2004. A restatement of the Mesozoic Atlasic Rifting (Morocco). *Journal of African Earth Sciences* 38, 145–153. https://doi.org/10.1016/j.jafrearsci.2003.12.003

Loudaoued, I., Touil, A., Aysal, N., Aissa, M., Keskin, M. & Ouadjou, A., 2023. Volcanic rocks from Amensif-Tnirt district in the Western High Atlas (Morocco): Geochemistry, magma features and new age dating. *Journal of African Earth Sciences* 205. https://doi.org/10.1016/j.jafrearsci.2023.104975

Loughlin, W.P., 1991. Principal component analysis for alteration mapping. *Photogrammetric Engineering & Remote Sensing* 57, 1163–1169.

Mabkhout, F., Bonin, B., Ait Ayad, N., Sirna, C. & Lagarde, J.-L., 1988. Les massifs granitiques alcalins du Permien marocain. *Comptes Rendus de l'Académie des Sciences. Serie 2,* 307, 163–168.

Missenard, Y., Taki, Z., Frizon de Lamotte, D., Benammi, M., Hafid, M., Leturmy, P. & Sébrier, M., 2007. Tectonic styles in the Marrakesh High Atlas (Morocco): The role of heritage and mechanical stratigraphy. *Journal of African Earth Sciences* 48, 247–266. https://doi.org/10.1016/j.jafrearsci.2007.03.007

Moore, G. & Frederick, W., 1986. Objective procedure for lineament enhancement and extraction. *American Society of Photogrammetry* 49, 641–647.

Ouanaimi, H., Fekkak, A., Ettachfini, E.M., Jouhari, A. & Aarab, A., 2018. *Explicative de la carte géologique du Maroc (1/50.000)* [*Explanatory of the geological map of Morocco (1/50,000)*]. Service Géologique du Maroc, 590 pp.

Permingeat, F., 1957. *Le gisement de molybdène, tungstène et cuivre d'Azegour (Haut – Atlas). Etude pétrographique et métallogénique* [*The molybdenum, tungsten and copper deposit of Azegour (High Atlas). Petrographic and metallogenic study*]. Notes et Mémoires du Service Géologique, Maroc, 141 pp.

Piqué, A., Tricart, P., Guiraud, R., Laville, E., Bouaziz, S., Amrhar, M. & Ouali, R.A., 2002. The Mesozoic-Cenozoic Atlas belt (north Africa): An overview. *Geodinamica Acta* 15, 185–208. https://doi.org/10.1080/09853111.2002.10510752

Pour, A.B. & Hashim, M., 2011. Identification of hydrothermal alteration minerals for exploring of porphyry copper deposit using ASTER data, SE Iran. *Journal of Asian Earth Sciences* 42, 1309–1323.

Pour, A.B. & Hashim, M., 2012. Identifying areas of high economic-potential copper mineralization using ASTER data in the Urumieh-Dokhtar Volcanic Belt, Iran. *Advances in Space Research* 49, 753–769.

Qaid, A.M. & Basavarajappa, H.T., 2008. Application of otimum index factor technique to Lansat-7 data for geological mapping of North East of Hajjah, Yemen. *American-Eurasian Journal Scientific Research* 3, 84–91.

Qarbous, A., Medina, F. & Hoepffner, C., 2003. The Tizi n'Test basin (High Atlas, Morocco): an example of extensional evolution of rifting of the Central Atlantic of the Triassic. *Canadian Journal of Earth Sciences* 40, 949–964. https://doi.org/10.1139/e03-029

Qarbous, A., Medina, F. & Hoepffner, C., 2008. Tectonique cassante et état de contrainte dans le bassin de Tizi n'Test (Haut Atlas, Maroc) au cours de l'inversion tertiaire [Brittle tectonics and state of stress in the Tizi n'Test basin (High Atlas, Morocco) during the Tertiary inversion]. *Estudios Geológicos* 64, 17–30.

Rajendran, S., Nasir, S., El-Ghali, M.A.K., Alzebdah, K., Al-Rajhi, A.S. & Al-Battashi, M., 2018. Spectral signature characterization and remote mapping of oman exotic limestones for industrial rock resource assessment. *Geosciences* 8, 145. https://doi.org/10.3390/geosciences8040145

Ricou, L.E., 1994. La Thétys reconstruite: plaques, blocs continentaux et leurs limites depuis 260 ma de l'amérique centrale à l'asie du sud-est [The Thetys reconstructed: plates, continental blocks and their limits since 260 mya from Central America to Southeast Asia]. *Geodinamica Acta 7*, 169–218. https://doi.org/10.1080/09853111.1994.11105266

Taib, Y., Touil, A., Aissa, M., Hibti, M., Zouhair, M. & Ouadjou, A., 2020a. *Pétro-géochimie des roches volcaniques et gîtologie de la minéralisation polymétallique (Cu-Zn-Pb ± Ag, Au) de Taourirte (Haut-Atlas Occidental, Maroc)* [*Petro-geochemistry of volcanic rocks and depositology of polymetallic mineralization (Cu-Zn-Pb ± Ag, Au) of Taourirte (Western High Atlas, Morocco)*]. Université Cadi Ayyad-Marrakech, 213 pp.

Taib, Y., Touil, A., Aissa, M., Hibti, M., Zouhair, M. & Ouadjou, A., 2020b. Geochemistry and petrogenesis of early Ediacaran volcanic rocks from taourirte district (Western High Atlas, Morocco): Origin and geodynamic implications. *Journal of African Earth Sciences* 170, 103936. https://doi.org/10.1016/j.jafrearsci.2020.103936

Teixell, A., Arboleya, M.L., Julivert, M. & Charroud, M., 2003. Tectonic shortening and topography in the central High Atlas (Morocco). *Tectonics* 22, 5, 1051, https://doi.org/10.1029/2002TC001460

Teixell, A., Ayarza, P., Zeyen, H., Fernàndez, M. & Arboleya, M.L., 2005. Effects of mantle upwelling in a compressional setting: The Atlas Mountains of Morocco. *Terra Nova* 17, 456–461. https://doi.org/10.1111/j.1365-3121.2005.00633.x

Thome, K., Palluconi, F., Takashima, T. & Masuda, K., 1998. Atmospheric correction of ASTER. *IEEE Transactions on Geoscience and Remote Sensing* 36, 1199–1211. https://doi.org/10.1109/36.701026

van der Meer, F., Hecker, C., van Ruitenbeek, F., van der Werff, H., de Wijkerslooth, C. & Wechsler, C., 2014. Geologic remote sensing for geothermal exploration: A review. *International Journal of Applied Earth Observation and Geoinformation* 33, 255–269. https://doi.org/10.1016/j.jag.2014.05.007

van der Werff, H. & van der Meer, F., 2016. Sentinel-2A MSI and Landsat 8 OLI provide data continuity for geological remote sensing. *Remote Sensing* 8, 883. https://doi.org/10.3390/rs8110883

Zoheir, B., El-Wahed, M.A., Pour, A.B. & Abdelnasser, A., 2019. Orogenic gold in transpression and transtension zones: Field and remote sensing studies of the Barramiya-Mueilha sector, Egypt. *Remote Sensing* 11, 2122. https://doi.org/10.3390/rs11182122

Manuscript submitted: 25 December 2023
Revision accepted: 25 May 2024